J. Phys. D: Appl. Phys. **46** (2013) 325303 (10pp) doi:10.1088/0022-3727/46/32/325303

Ag^+ release inhibition from ZrCN–Ag coatings by surface agglomeration mechanism: structural characterization

S Calderon V[1], R Escobar Galindo[2], N Benito[4], C Palacio[4], A Cavaleiro[3] and S Carvalho[1]

[1] Universidade do Minho, Dept. Física, Campus de Azurém, 4800-058 Guimarães, Portugal
[2] Instituto de Ciencia de Materiales de Madrid (ICMM -CSIC), Cantoblanco, 28049, Madrid, Spain
[3] SEG-CEMUC Mechanical Engineering Department, University of Coimbra, 3030-788 Coimbra, Portugal
[4] Departamento de Física Aplicada, Universidad Autónoma de Madrid, 28049, Madrid, Spain

Received 13 February 2013, in final form 7 June 2013
Published 17 July 2013
Online at stacks.iop.org/JPhysD/46/325303

Abstract
New multifunctional materials based on well-established materials to which functional properties are added, such as antibacterial performance, have become a relevant research topic, in order to meet the requirements of today's technological advances. This paper reports the results of a detailed structural and chemical characterization study of ZrCN–Ag coatings produced by reactive magnetron sputtering, as well as the release of silver after immersion in a simulated body fluid (Hank's balanced salt solution), which mimic the material behaviour within the human body. The chemical composition was evaluated by electron probe microanalysis, x-ray photoelectron spectroscopy and Rutherford backscattering spectroscopy, whereas the structure was assessed by Raman spectroscopy and x-ray diffraction. The material exhibits a homogeneous distribution of the elements throughout the films, with a (C + N)/Zr ratio of around 1.3 and 15 at% of silver. A mixture of amorphous (a-C and CN_x) and crystalline phases (ZrCN) was identified. In addition, the silver was detected to be released in less than 0.7% of the total silver in the films, occurring during the first two hours of immersion; no further release was evidenced after this period of time.

(Some figures may appear in colour only in the online journal)

1. Introduction

The development of new materials involves not only a proper combination of elements but also an appropriate material architecture design, depending radically on the application to which the product will be used. However, certain characteristics such as high quality, efficiency and durability should be predominant features that a material must possess nowadays. Transition-metal carbonitrides are good example of these materials; widely appreciated due to their capacity to extend the lifetime of many industrial tools and to improve mechanical properties, thanks to their high hardness, corrosion resistance, high melting point, low coefficients of friction and abrasion resistance [1–7]. ZrCN, for instance, although rarely used for technological application as a bulk material, has in the last decade become very attractive in the form of thin films due to their remarkable mechanical, tribological, chemical, decorative and biocompatibility properties [8–11]. ZrCN hardness has been reported in a wide range of values, starting from a few GPa up to values as good as 35 GPa, depending on the architecture of the material (thin films, multilayers, among others) and its combination with others elements [8, 9]. These ternary materials also have good bio-related properties, having demonstrated their potentiality for medical devices. Balaceanu *et al* [7] have shown that Zr/ZrCN multilayer coatings with low carbon content may be promising for biomedical applications, substantially improving the biocompatibility of stainless steel 316L implants. Khan *et al* [12] on the other hand showed that ZrCN films were attractive as surgical tools due to their biocompatibility with the human body, enhancing the fatigue lifetime of the components. Hollstein *et al* [13] have demonstrated that ZrCN films are more chemically resistant

 © 2013 IOP Publishing Ltd Printed in the UK & the USA

than those based on Ti and that a variety of ZrCN films have fulfilled the requirements for short-term applications in the human body.

Despite all the characteristics depicted for ZrCN films, additional features such as antibacterial capabilities are demanded in the field of biomaterials. However, to the authors' knowledge only one report has been published regarding this topic. Lai *et al* [14] deposited ZrCN/a-C composite coatings with significant short-term antibacterial effect. However, in order to better exploit the ZrCN characteristic, this effect must become a long-term property in order to be used in applications such as orthopaedic prosthesis, catheters and stents, among others. For that reason, the introduction of an antibacterial agent which helps the system to maintain a steady bactericidal effect for longer periods of time might solve this problem.

Silver, has been extensively studied and is known as an efficient and effective antibacterial agent [15–21]. Nonetheless, the durability of the effect is ignored in most of the reports, precluding their use in long-term applications. Thus, this effect stability gains particular importance when dealing with applications involving the human body since the reduction of this effect as a function of time could expose the material to a normal colonization and became a non-antibacterial material. The majority of studies report a quick release of silver ions during the first days of contact of the material with the simulated body fluids. A reduction of Ag^+ release was observed after a few days for very low values, generally for less than 15 days of immersion [18, 22, 23]. Nevertheless, no explanation was found for such phenomena.

Thus, with the aim of better understanding the mechanisms behind the silver ion release from complex matrices, this work presents the characterization of ZrCN film with silver nanoparticles synthetized by reactive dual magnetron sputtering and evaluates the silver release after immersing the samples into Hank's balanced salt solution (HBSS) electrolyte that simulates the body fluids. Special attention will be focused on the understanding and description of the structural characteristics of ZrCN with silver nanoparticles, as well as on the material ability to produce silver ions, with the purpose of controlling ions release and being able to manage the antibacterial effect and the cytotoxicity of the material.

2. Materials and methods

2.1. Coatings production

Zirconium carbonitride coatings with silver nanoparticles (ZrCN–Ag NPs) were deposited onto 316L stainless steel (SS316L) and Si (1 0 0) substrates, using a dual magnetron sputtering system equipped with a rotating substrate holder system, employing two 99.8% Zr targets. In order to introduce the silver nanoparticles, one Zr target was modified with silver pellets distributed along the target erosion zone, maintaining a Zr/Ag area ratio around 3. The base and working pressures of the deposition were kept around 8.7×10^{-4} Pa and 2.1×10^{-1} Pa, respectively. The rotation speed of the substrate holder was maintained at 8 rpm to achieve homogeneous films. Before the deposition, a cleaning pre-treatment of the substrates was performed in order to guarantee the adhesion of the films, consisting in removing the dust and degreasing the surface with ultrasonic baths using ethanol, acetone and distilled water during 10 min for each fluid. Thereafter, samples were etched in an Ar atmosphere for 1200 s. A zirconium interlayer was deposited, ensuring a proper interface between the stainless steel and the ZrCN–Ag layer. Finally, the ZrCN–Ag NPs multifunctional layer was added to the system using 60 sccm Ar flux, 4 sccm of N_2 and 1.2 sccm of C_2H_2, keeping Zr–Ag and Zr target density currents at 2.5 mA cm^{-2} and 7.5 mA cm^{-2}, respectively. The chamber temperature (573 K), bias voltage (−50 V), targets voltage and pressure were monitored and kept constant during the entire experiment.

2.2. Chemical and physical characterization

After deposition, samples were analysed by a Cameca SX 50 electron probe micro-analyser (EPMA) with the purpose of determining the coating chemical composition. X-ray diffraction (XRD) was employed to reveal information about the film crystalline structure, using a Siemens diffractometer with Co Kα 1.78897 Å radiation in grazing angle mode. Additionally, and due to the high tendency of C and N to form amorphous phases in these types of films [2, 8, 14, 24], a Renishaw InVia Microscope with an excitation light of Ar 514.5 nm laser was employed to obtain Raman spectra in order to identify these phases.

Rutherford backscattering spectrometry (RBS) was performed with the aim of evaluating in-depth compositional profile of the coatings, due to the fact that this technique presents a high elemental sensitivity for heavy elements. The experiments were carried out by means of a 5 MV HVEE Tandetron at the Centro de Micro-Análisis de Materiales of Universidad Autónoma de Madrid. The RBS spectra were collected with He ions at an ion dose of 10 μC and energies range between 3.68 and 3.80 MeV. The analysis at different ion energies provides complementary information about the coatings structure. The data were acquired simultaneously with two silicon surface barrier detectors located at scattering angles of 170° and 165°, respectively, with an energy resolution of 16 keV. The experimental spectra were fitted using the program RBX [25].

Finally, x-ray photoelectron spectroscopy (XPS) spectra were measured in an ultrahigh vacuum system at a base pressure below 8×10^{-8} Pa using a hemispherical analyser (SPECS Phoibos 100 MCD-5). The pass energy was 9 eV giving a constant resolution of 0.9 eV. The Au $4f_{7/2}$, Ag $3d_{5/2}$ and Cu $2p_{3/2}$ lines of reference samples at 84.0 eV, 368.3 eV and 932.7 eV, respectively, were used to calibrate binding energies. A twin anode (Mg and Al) x-ray source was operated at a constant power of 300 W using Mg Kα radiation. For samples cleaning, ion bombardment was carried out using a penning ion source (SPECS IQP 10/63) with an angle of 45° between the normal to the surface and the ion gun axis, and an ion beam energy of 3 keV, raising the pressure to 4×10^{-2} Pa of Ar^+. The ion beam current density, measured with a collector that can be placed in the same position as the sample holder,

Table 1. ZrCN–Ag NPs composition obtained by EMPA and RBS.

	Composition (at%)				
	Zr	N	C	O	Ag
EPMA	32.2	28.3	19.1	10.3	11.1
RBS	34.0	28.0	13.0	10.0	15.0

Note: Results possess standard deviation between 0.2 and 0.8 for EPMA and 0.5 and 1.2 for RBS.

was 4.6 μA cm^{-2}. Those experimental conditions lead to an ion beam with a flat profile greater than $\sim$10 $\times$ 10 mm^2.

2.3. Silver ion release

Samples of 1.7 cm^2 were immersed into 200 ml of HBSS and their compositional depth profile was evaluated after 0, 2, 48 and 168 h of immersion by RBS and glow discharge optical emission spectroscopy (GDOES). The GDOES experiments were utilized to evaluate the compositional profile of the as-deposited samples and after immersion, allowing the prediction of silver distribution and evolution along the experiment. The tests were performed using a Jobin Yvon RF GD Profiler equipped with a 4 mm diameter anode and operating at a typical radio frequency discharge pressure of 650 Pa and a power of 40 W. Additionally, film surface was evaluated in order to detect small variation in the composition and morphology. The morphology was assessed using a NanoSEM-FEI Nova 200 scanning electron microscopy while surface chemical composition and bonding were assessed by XPS, acquired by using the experimental setup explained in the structural methodology, without sputtering the samples in order to obtain the effect of the electrolyte on the surface.

Finally, the fluids were analysed by means of an inductively coupled plasma mass spectrometer (ICP-MS) to evaluate the accumulation of silver ions in the electrolyte.

3. Results and discussion

3.1. Chemical composition

The films compositions were obtained by EPMA and RBS techniques and are presented in table 1. Due to the complexity of the RBS modelling for a compound consisting of 4 elements, the EPMA results were used to define the start point for RBS fitting model. Both techniques gave considerably similar results, in which the main differences are found in the C and Ag content. The results revealed not only the presence of Zr, C, N and Ag but also the existence of oxygen in the films. In fact, this oxygen may come from residual oxygen in the deposition chamber during the production, as well as a small amount due to natural surface oxidation that uncontrollably occurs on metals such as Zr in contact with moisture in the environment [26].

The profile composition obtained after fitting RBS results shows a constant composition throughout the film, up to the zirconium interlayer, in which the combination of zirconium with the elements from the functional films is noticed, mainly due to the roughness of the substrate (65 nm). Figure 1 shows an example of the RBS spectrum with its corresponding fitting result.

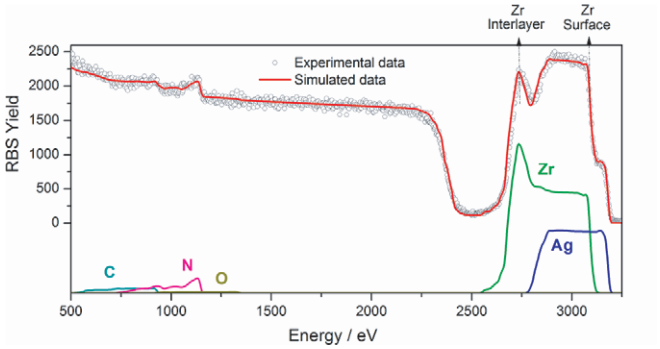

Figure 1. RBS spectra for ZrCN–Ag NPs at 3.68 MeV.

The composition shown in table 1 revealed an excess of carbon and nitrogen in relation to the Zr content with (C+N)/Zr ratio around 1.3, suggesting that not only may crystalline ZrCN phases be present in the films, but also C and CN_x amorphous phases, later confirmed by XRD and Raman spectroscopy. This mixture of phases could beneficiate the tribological and mechanical properties of the films, inducing reduction in the coefficient of friction due to the formation of the amorphous phases as reported by Silva *et al* [8]; in addition, the ratio between the C/N implemented in this work has been reported by others groups [27] to increase the microhardness of such materials; however, due to the formation of the mentioned amorphous phases and the presence of a soft metallic phase (Ag), the hardness of this material is not expected to be very high.

Furthermore, in such a complex matrix, several possible element combinations can be expected, among which both amorphous phases such zirconium oxide, carbon and carbonitrides, as well as, crystalline phases such as zirconia, zirconium carbide, nitride or carbonitride and oxynitride can be present. Thus, in order to better understand the phases presented on the films, XRD, Raman spectroscopy and XPS were conducted.

3.2. X-ray diffraction

XRD spectrum is shown in figure 2. The material possesses a well-defined crystalline phase with a face-centred cubic (fcc) structure B1 typical of ZrCN. The diffractogram shows a preferential (1 1 1) orientation, with the peak located between the ZrC and ZrN reference peaks, which demonstrates a complete miscibility of these phases, forming a solid solution of ZrCN [1, 28]. In addition, oxygen at low amounts can substitute nitrogen/carbon atoms or be located at interstitial sites in the fcc crystal, implying a lattice distortion and formation of non-uniform microstress [29].

ZrCN compounds have been found to obey Vergard's rule [1], where the lattice parameters from the forming binary compounds can be combined in a linear manner to obtain the lattice parameter of the ternary compound, as shown in equation (1). It correlates the lattice parameter and the ratio

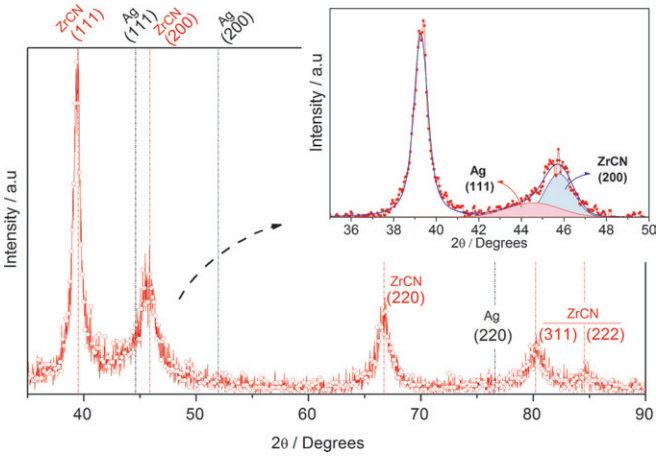

Figure 2. ZrCN–Ag NPs XRD spectra.

between the carbon and nitrogen content in the crystalline phase,

$$a_{\mathrm{ZrCN}} = a_{\mathrm{ZrN}}\,(1 - x) - a_{\mathrm{ZrC}}x \qquad (1)$$

where a is the lattice parameter and x is the carbon concentration in relation to the C+N concentration (C/(C+N)). Using this relation, it is possible to estimate the carbon and nitrogen associated with the ZrCN phase. Thus, calculating the x value from equation (1), the C/(C+N) ratio is established around 0.3, which represents a phase with 30% of C and 70% of N linked to the ZrCN. Therefore, the nitrogen and carbon excess could represent the amount of amorphous phase formed by those two elements. Nevertheless, special care must be taken since Zr is not expected only to be bonded to ZrCN. The presence of oxygen may induce the formation of other types of compounds such as ZrO_2 in an amorphous phase and/or interstitial oxygen could be found into the ZrCN lattice. In the first case, the effect on the previous calculation is to increase N and C excess available to form the amorphous C and CN_x phases, maintaining the C/(C + N) ratio. In the second case, the interstitial oxygen would produce a slight shift in Bragg's angle to higher angles, signifying a decrease in the lattice parameter which in turn increases the C/(C+N) from Vergard's relation, without affecting the amount of C + N available for the amorphous phase formation. Therefore, in order to obtain a better comprehension and occurrence of these situations, further analyses were carried out by Raman spectroscopy and XPS and are presented in their respective sections.

Silver, on the other hand, did not show a well-defined crystalline phase in the XRD spectrum. The deconvolution of the peak around 45° leads to the determination of two peaks. At 45.7° the peak belongs to the (2 0 0) plane of ZrCN while the other peak at 44.6° corresponds to the (1 1 1) plane of silver (ICDD 01-087-0719). The grain size of silver phase calculated by means of Scherrer's formula is around 3.4 nm.

Figure 3 shows the morphology of the film obtained by SEM. Three magnifications are shown for analysing the surface of the samples, as well as the cross-section of the coating. It may be seen in figure 3(*a*) that the film adopts the surface morphology of the substrate, displaying the steel grain boundaries. However, a closer look to the surface unveils a granular surface of the film itself. Figure 3(*b*), obtained using a backscattered electrons detector, shows a slight difference in brightness of a few spots on the surface. This contrast might signify differences in mass between particles, in which the brightest element may represent the silver particles. However, energy dispersive x-ray analysis (EDS) did not reveal any significant differences between zone 1 (Z1 figure 3(*b*)) and zone 2 (Z2 figure 3(*b*)) mainly attributed to the size of the particles and the resolution of the method, leading us to conclude that there is a homogeneous distribution of the silver over the material surface. The cross-sectional image (figure 3(*d*)) revealed significant differences between the Zr interlayer, with a columnar growth, and the functional layer where a granular morphology is detected. This granular behaviour is believed to be promoted by the silver nanoparticles together with the amorphous phases [30, 31] that limit the directional growth of the films by forming small grains within the ZrCN grains. In addition, the small particles on the material surface are also observed on cross-sectional images, with sizes lower than 20 nm. Finally, it may be concluded that the silver is well distributed along the surface, as well as on the films' profile without evidence of silver agglomeration and/or precipitation to the surface of as-deposited samples; such segregation has been reported in similar materials [24, 32].

3.3. Raman spectroscopy

C–C bonds were identified by Raman spectroscopy (figure 4), revealing amorphous carbon phases in the films. At 1336 cm^{-1} and 1570 cm^{-1} the signal corresponding to the D (disordered) and G (graphitic) band of the carbon are observed, respectively [5]. The former is attributed to the bond angle disorder in the graphite-like phase, while the latter is identified as the graphite layers of sp^2 bonds [12]. Kurt [33] also explains that D band could appear due to the finite size of the graphite domains and originates from grain boundaries or imperfections, such as substitutional N atoms, sp^3 C or other impurities. Zheng states that the G band arises from the symmetric e_{2g} levels [34]. Therefore, these two peaks reveal a highly disordered structure as expected for an amorphous carbon. On the other hand, similar to the vibrational modes of the graphite, the ZrN forbidden bands (the first order Raman scattering) are observed due to the disorder and imperfection of the structure [29]. Moura *et al* showed the presence of a principal peak of ZrN around 500 cm^{-1} attributed to the asymmetric band [29], peak which was also found in the material studied in this work but slightly shifted to lower frequencies probably due to the compressive stress and the lattice dynamics. In addition, the presence of a small shoulder at higher frequencies (580 cm^{-1}) may be attributed to the presence of oxygen in the structure [29], as confirmed by XPS.

3.4. X-ray photoelectron spectroscopy

Binding energies results for different types of bonds are shown in figure 5 and table 2, as well as binding energy reported by other researchers. The peak at 284.8 eV is attributed to the carbon linked to carbon, revealing the amorphous carbon phase that was expected due to the composition of the films

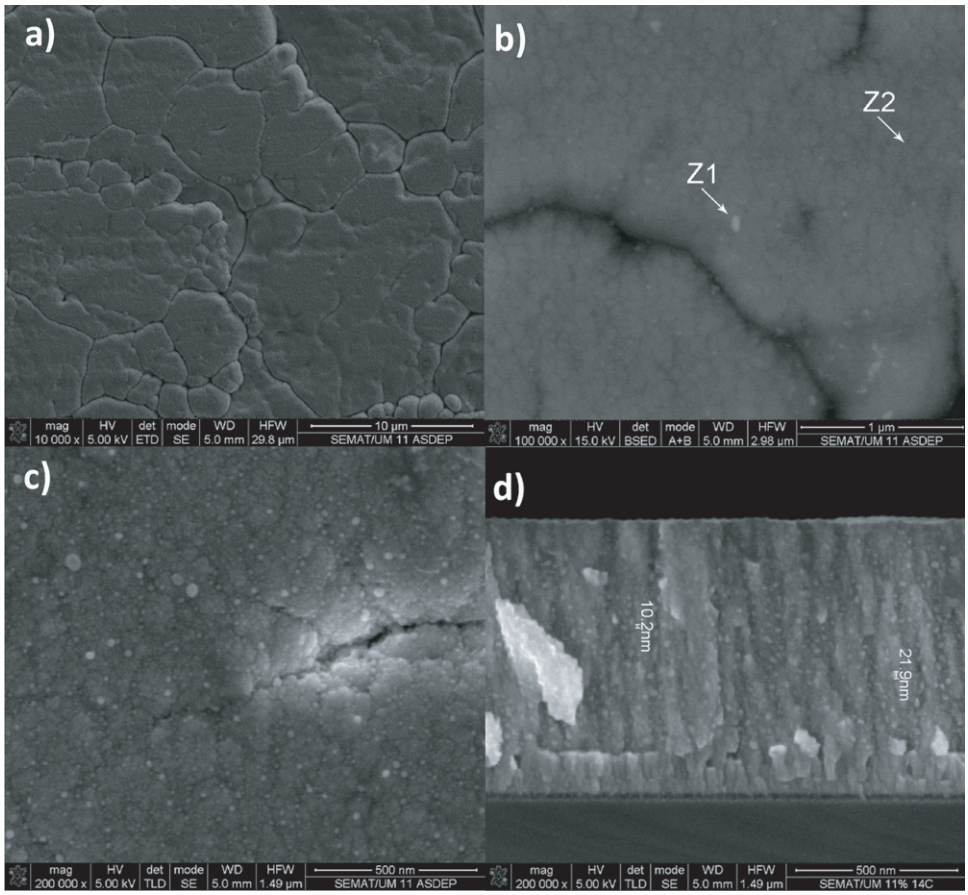

Figure 3. ZrCN–Ag NPs SEM images (*a*) surface image at 10 k×, (*b*) surface image at 100 k× using backscattering mode, (*c*) 200 k× and (*d*) cross-sectional at 200 k×.

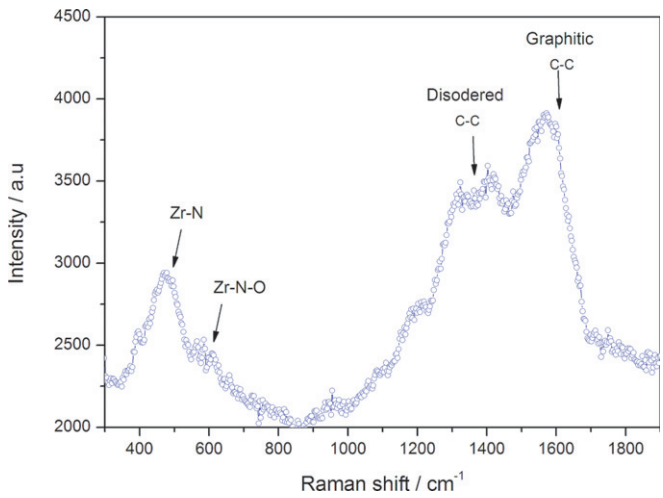

Figure 4. ZrCN–Ag NPs Raman spectra.

and later confirmed by Raman spectroscopy. Furthermore, C–Zr bonds were identified at 282.5 eV. This is consistent with the component observed at 179.8 eV in the Zr 3d band. The C1s band shows also an additional feature at 286.1 eV; this peak should be attributed either to C sp^2–N and C–O bonds which could indicate both interstitial oxygen in the ZrCN structure and CN_x amorphous phases [35]. These bonds were confirmed in the O 1s and N 1s range of energies in which peaks for energies near to 532.7 eV previously reported for O–N and O–C bonds [36] and 400.2 eV revealing N–O, and therefore, discarding N–C sp^3 bonds that are not observed in the C spectrum. In addition a peak close to 399.0 eV was evidenced, confirming the N–C sp^2 bonds.

The results allow calculating the ratio between the Zr–C/(Zr–C + Zr–N), finding similar results compared with Vergard's equation in the XRD section, showing a compound with the following stoichiometry $ZrC_{0.35}N_{0.65}$, as seen in table 2. Thus, the crystalline phase is a phase in which around 35% of the N atoms were substituted by carbon atoms forming a solid solution. However, the amount of the amorphous phases evidenced by N–C (399.0 eV) and C–C (284.4 eV) bonds cannot be accurately estimated, due to the amount of oxygen present in the material surface, and therefore, only rough estimations about the ration between the crystalline and the amorphous phases can be performed. Thus, considering the bonds between the zirconium with carbon and nitrogen and the bonds between carbon with carbon and nitrogen, it was possible to calculate that the total (ZrCN crystalline phase)/(a-C + C–N amorphous) is around 1.3. This ratio between the phases can play a very unique role in mechanical, tribological and corrosion resistant properties of the films, since it is well know that the amorphous phases can decrease the coefficient of friction, as well as alter the hardness and young modulus of the film [8]. Anyway, concentration calculations by XPS should not be overemphasized because the previous sputtering

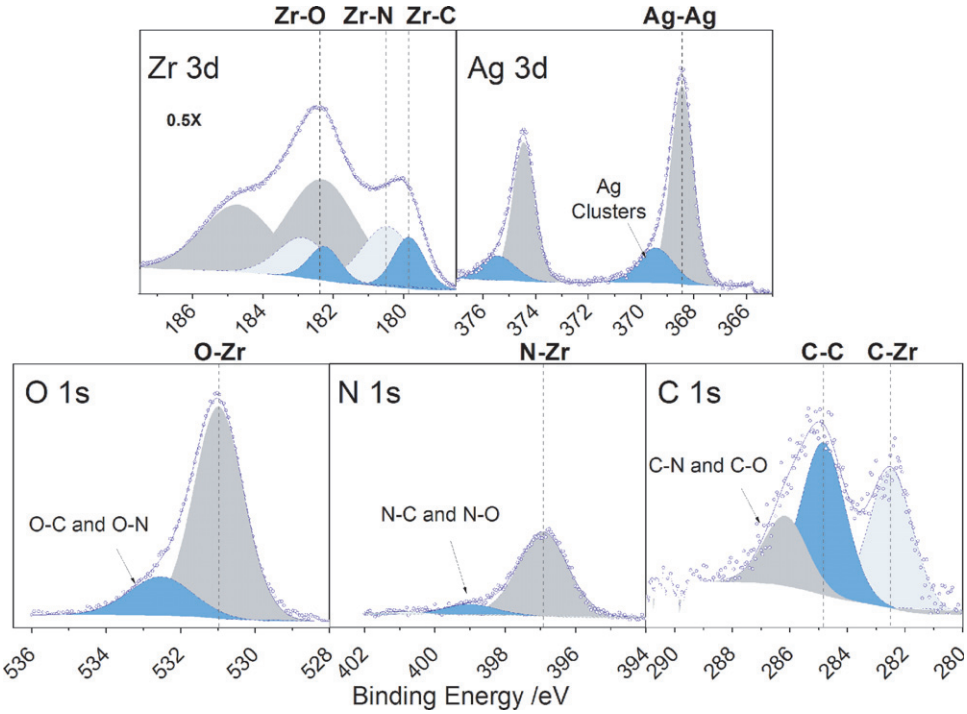

Figure 5. XPS spectra of Zr d3, Ag d3, O1s, N1s and C1s core levels of ZrCN–Ag NPs coatings after 10 min of sputtering.

Table 2. Binding energies of the C 1s, O 1s, Zr 3d ,O 1s and Ag bands found for the samples after 10 min of sputtering and reference.

Bond type	Binding energy (eV)	at%	References binding Energy (eV)	Reference
C–C	284.8	6.7	284.4, 284.5	[9, 15]
C–O and C–N	286.1	3.1	285.2–285.5, 286.3	[9, 15]
C–Zr	282.5	6.2	281.6, 282.2–282.4, 281.9	[2, 9, 15]
O–Zr	531.0	20.3	531.5	[38]
O–N and O–C	532.7	4.4	533.6	[38]
Zr–C	179.8	5.2	179.2, 179.5	[2, 9]
Zr–N	180.5	9.9	180.0, 180.0, 179.9	[9, 15, 38]
Zr–O	182.3	23.3	182.0–183.2, 182.2	[9, 38]
N–C	399.0	1.8	399.4, 400.6	[9]
N–Zr	397.0	14.3	397.2, 397.0–397.1, 397.2	[2, 9, 15]
N–O	400.8	0.3		
Ag–Ag	368.4	3.5	368.3 eV	[25]
$Ag_{Cluster}$	369.4	1.0		

treatment carried out to remove adventitious carbon could lead to preferential sputtering of light elements of such a complex compound.

As was mentioned before, Zr might easily form ZrO_2 with the environment on the material surface, a fact that can explain the high amount of oxygen in the XPS results, which may disagree with the bulk composition analysis of the material since the technique only assesses the first few layers of the samples (∼2.5 nm if Zr 3d photoelectrons are being analysed). The results showed a large portion of the zirconium linked to oxygen (182.3–182.4 eV), expressing the high reactivity of this material and its ability to form passive layers, which in turn could be beneficial to properties such as corrosion resistance.

For Ag 3d, a broad band at ∼369.4 eV was detected in addition to the metallic peak at 368.4 eV. Some authors have attributed this band to metallic sub-nanoparticles associated with clusters smaller than 4 nm [37, 38]. This band has been shown to change its position and form depending on the cluster sizes and distribution. The width observed in this work (∼1.6 eV FWHM) points to a large distribution of cluster sizes, while the metallic silver peak is positioned at the energy reported by several authors [24], as presented in table 2. The peak related to Ag-clusters has been detected before and after sputtering, but with different metallic/cluster ratio. For samples before sputtering, almost 92% of the silver is metallic, while after sputtering this percentage decreases to 79%. This cluster amount reduction at the surface is believed to be essential in the silver ion release of the films and will be further discussed in the silver dissolution.

3.5. Silver ion release

The chemical composition evolution of the films before and after the immersion in HBSS evaluated by RBS did not evidence significant changes. The spectra were fitted using the same layer model, obtaining compositions presented in

Table 3. Fitting results from RBS results as a function of immersion time for two different depths.

		Compositions RBS (at%)				
Depth	Immersion time	Zr	N	C	O	Ag
250 nm	168 h	34	28	13	10	15
	0 h	34	28	13	10	15
0 nm	168 h	34	30	14	10	13
	0 h	33	29	14	10	14

table 3. Composition at 250 nm and on the surface of the films is presented, revealing very stable films after immersion, decreasing 1 at% of the silver on the material surface after 168 h. Nonetheless, the differences between the samples are within the measurement error of the technique, and hence, it is impossible to conclude that any silver release is reached after immersion, and therefore, more precise techniques were necessary to evaluate the evolution of the silver after immersion. Thus, in order to better show the change in silver composition in the films GDOES, XPS and ICP results are presented.

Figure 6 shows the depth profile composition of the films obtained by GDOES. The profiles of the samples after immersion are very similar to as-deposited ones confirming the results from RBS. In addition, a thin layer of silver located on top of an oxide layer is revealed, which was reduced after the samples were immersed into HBSS, as shown in figure 7(*a*). A decrease of the top silver films was observed after immersion, but in very low quantities, only in the first 2.5 nm of the surface. In addition to the silver, phosphorus (figure 7(*b*)) and sulfur (figure 7(*c*)) were detected by GDOES on the material surface after immersion, slightly increasing with increasing immersion time. Despite the fact that the reduction of the silver peak and the increment of the S and P peaks were evident for every sample after immersion, the amount of these elements was not calculated by GDOES since the results were considered to offer only qualitative information about the distribution of the elements in the film, as well as the evolution of the silver after immersion. Thus, in order to quantify the mentioned silver released, ICP was utilized using the fluid employed during RBS and GDOES experiments, showing that around 0.7% of the silver in the films was released, which corresponds to a 7 ppb cm^{-2}. This amount of silver corresponds to a 0.077 at% of the total composition of the films, explaining why the differences were not noticed by RBS in bulk analysis. It may also be stressed that the release of the silver was observed in the first two hours of contact with the fluid but after that time no further release is evidenced either by GDOES and ICP measurements. These results lead to the conclusion that silver ionizes in very low quantities and that only the silver on the material surface may be oxidized. The GDOES results reveal that sulfur and phosphorous penetration could indicate the maximum penetration of the electrolyte modifying the material, which partially explains the low release of silver to the medium since the S and P were only observed in the first 5–7 nm of the film. Nonetheless, not all the silver located in the first nm of the material was ionized, and hence, the existence of elements such as O, S and P may induce the formation of some

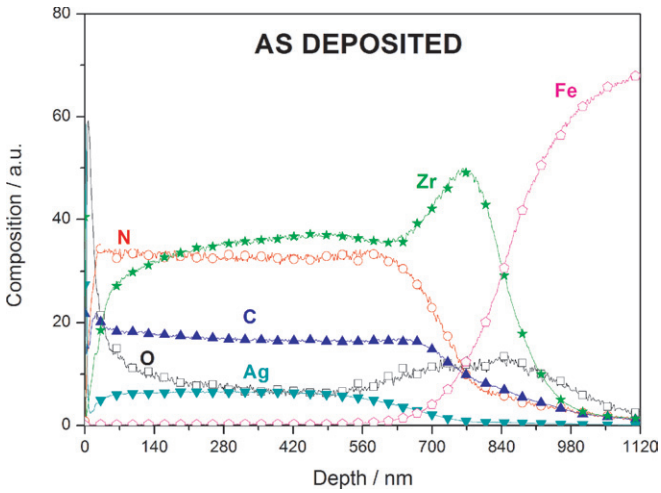

Figure 6. Compositional depth profile of ZrCN–Ag as-deposited samples obtained by GDOES.

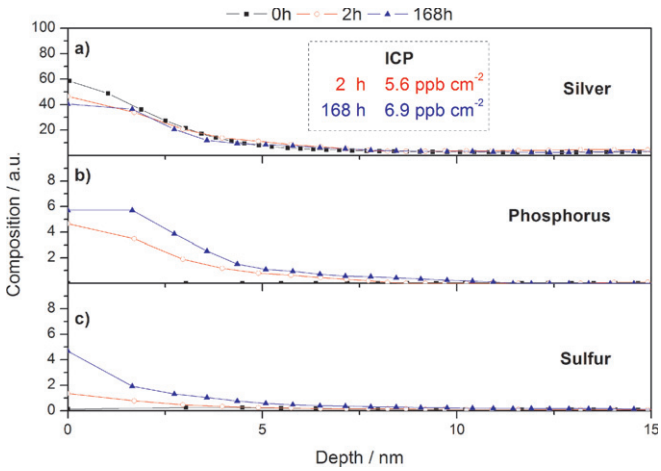

Figure 7. Silver, phosphorus and sulfur depth profile of ZrCN–Ag as a function of immersion time obtained by GDOES.

more stable silver compounds than the metallic nanoparticles silver such as sulfides, sulfates, phosphates and oxides. Thus, XPS analyses were carried out to clarify the results.

Figure 8 shows XPS spectra of samples before and after immersion. A clear sulfur appearance on the surface of the material is observed after contact with HBSS, which is likely to come from the $MgSO_4$ present in the electrolyte. However, the peak position around 162.3 eV revealed that the sulfur is probably forming a sulfide (S^{-2}), instead of a sulfate (SO_4^{-2}) whose energy has been reported close to 168.3 eV [37].

Based on XPS reports for Ag 3d bands [37], metallic silver compared with the different silver compounds such as $AgCO_3$, $AgNO_3$, Ag_2S and AgCl, $AgSO_4$ present very close binding energies. Only Ag oxides display binding energies 0.8 eV below the metallic peak. Therefore, the small peak observed near 367.1 eV should be associated with silver oxides, although the formation of Ag_2S cannot be ruled out, since the binding energies reported for Ag–Ag and Ag–S overlap [37]. Comparing these results with the XPS after sputtering presented in the XPS section for the structural characterization, a reduction in the metallic/cluster

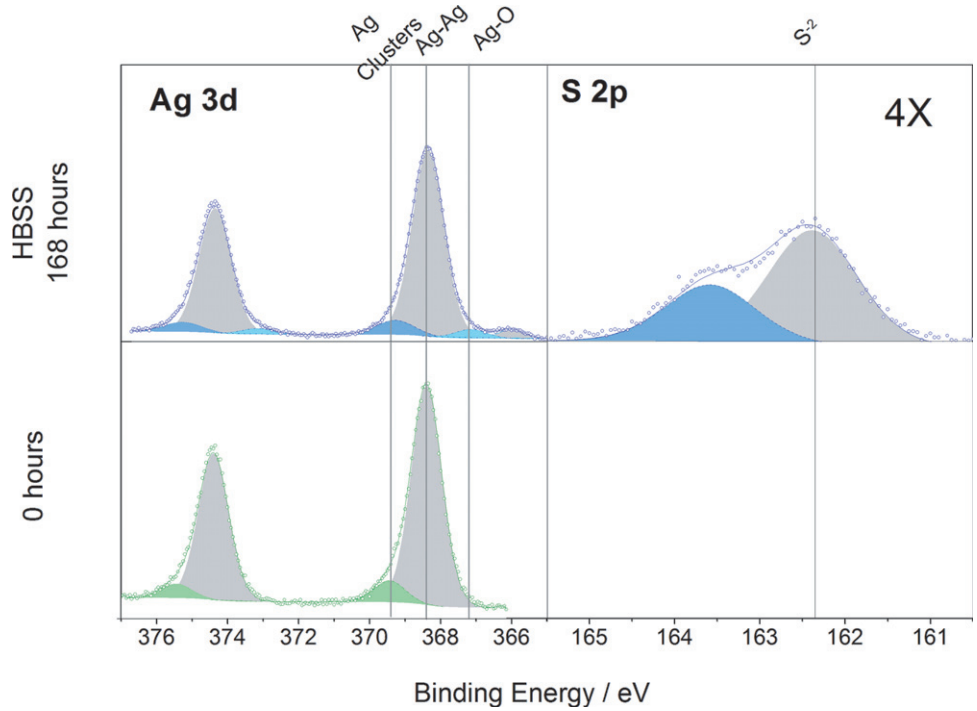

Figure 8. XPS spectra of Ag d3, and S 2p core levels of ZrCN–Ag NPs coatings after 0 h and 168 h of immersion in Hank's balance solution.

area ratio after Ar^+ bombardment is observed. Such reduction indicates an increase in the metallic form of the silver and a decrease in the clusters forming on the material surface, which also contributes to diminishing the silver ionization, since on decreasing the silver particle size the ionization is augmented, and therefore, the lower the clusters are on the surface, the lower is the silver ionization.

On the other hand, a redistribution of the silver on top of the films was observed as shown in the surface image of the samples before (figure 9(*a*)) and after 168 h immersion (figure 9(*b*)). The images were taken using backscattering electron detector, revealing the formation of particles with different composition to the film (white spots) with sizes below 300 nm as shown in figure 9(*c*). The differences in composition between the particles and the films were analysed by EDS and the results are shown in figures 9(*d*) and (*e*), respectively. The particles displayed a more intense peak of silver compared with the zirconium peak, revealing a larger amount of silver present in the area evaluated. However, the size of the spot and particles did not allow determining the proper composition of these particles. Furthermore, an EDS elemental map confirmed the concentration of silver in the zone of the brighter particles observed by SEM, as seen in figure 10. Nevertheless, the analysis of the isolated Ag map did not reveal any absence of silver localized in specific regions of the image, which confirms the lack of silver redistribution on the bulk material (600 nm). The results did not reveal the presence of Cl either by XPS or EDS spectra, discarding AgCl particles formation.

The formation of these particles on the film surface suggests that despite no silver being diffused throughout the films after immersion, it has some mobility on the surface that allows its redistribution and agglomeration. It is hypothesized that the silver ions produced on the surface of the material

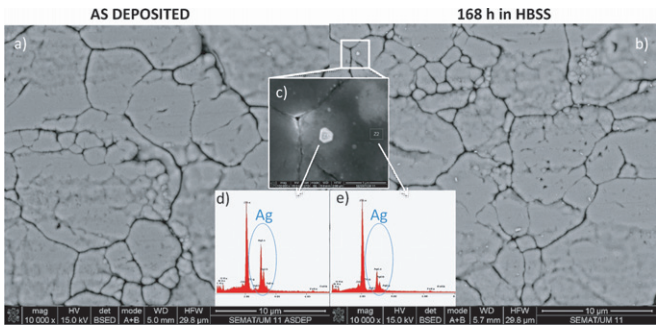

Figure 9. SEM images of ZrCN–Ag coatings (*a*) as-deposited, (*b*) after 168 h of immersion in HBSS, (*c*) after 168 h of immersion, (*d*) EDS of Z1 and (*e*) EDS of Z2.

form a thin layer of fluid with a high silver ion concentration which due to the neutral pH and the high ionic strength of the electrolyte leads to the silver ions aggregation [38], which in turn forms particles that start to grow as a function of time, as schematized in figure 11. Furthermore, it must be mentioned that the particles are linked to the surface of the material since the samples were cleaned in ultrasonic bath during 10 min in distilled water, indicating that the mentioned agglomeration may started on a silver particle remaining attached to the surface.

4. Conclusion

In this study, a novel type of metal-hard compound, namely ZrCN with silver nanoparticles (ZrCN–Ag NPs) has been successfully produced by magnetron sputtering. The material structure was identified as a mixture of crystalline and amorphous phases among which the $ZrC_{0.35}N_{0.65}$ is

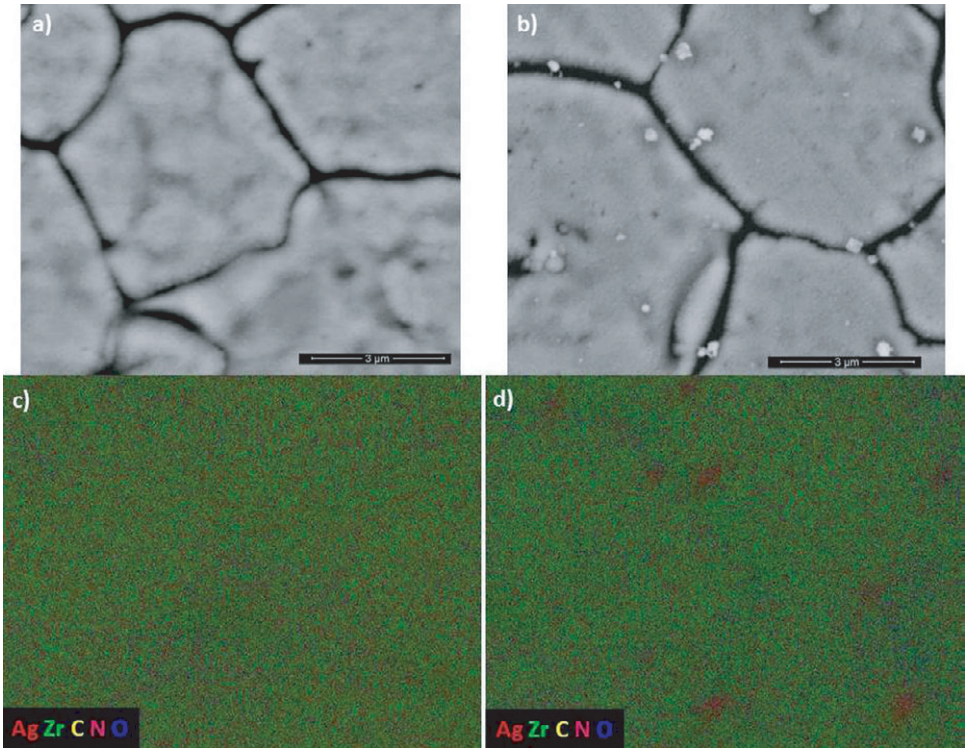

Figure 10. (*a*) and (*b*) SEM images of ZrCN–Ag before and after 168 h of immersion in HBBS, respectively. (*c*) and (*d*) EDS elemental map of ZrCN–Ag before and after 168 h of immersion in HBBS, respectively.

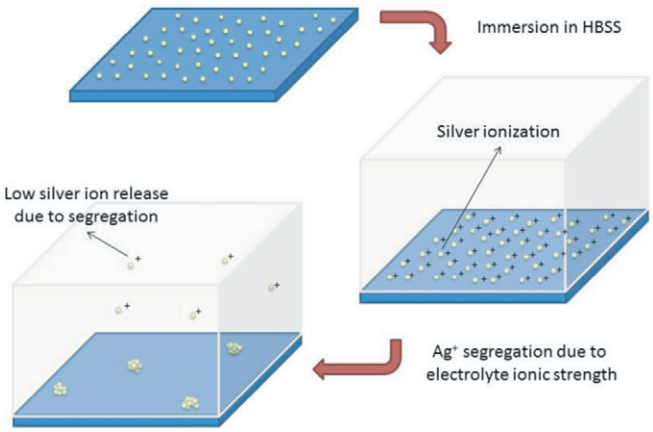

Figure 11. Silver agglomeration mechanism scheme.

highlighted as the predominant phase. However, additional phases such as a-C and CN_x amorphous phases were also identified. The silver was found in the form of nanoparticles embedded in the matrix, forming both clusters and metallic bonds, with a reduction of almost 13% of the cluster form on the surface compared to the interior of the film.

After the samples are in contact with the Hank's balance solution, only 0.7% of silver is released to the electrolyte during the first 2 h of immersion and no further release is noticed for 48 and 168 h of immersion. The electrolyte was observed to penetrate no further than 5 nm during the 168 h of immersion, which may prevent further silver ionization, working as a self-controlled material for silver release, favouring the use of such material for application in which wear of the material is expected. The wear, in such cases, may allow the electrolyte to interact with the silver located deeper in the films, activating new silver ion release. However, these mechanisms are to be assessed in further studies in order to be confirmed. In addition, the samples showed silver mobility and redistribution on the material surface but also without any extra silver ionization.

Acknowledgments

This research is partially sponsored by FEDER funds through the program COMPETE—Programa Operacional Factores de Competitividade and by Portuguese national funds through FCT-Fundação para a Ciência e a Tecnologia, under the projects ANTIMICROBCOAT—PTDC/CTM/102853/2008. This work has also been supported by the Ministerio de Ciencia e Innovación of Spain through the Consolider-Ingenio 2010 programme (CSD2008-00023) and through project RyC2007-0026.

References

[1] Larijani M, Zanjanbar M and Majdabadi A 2010 *J. Alloys Compounds* **492** 735–8
[2] Craciun D *et al* 2011 *Appl. Surf. Sci.* **257** 5332–6
[3] Lengauer W *et al* 1995 *J. Alloys Compounds* **217** 137–47
[4] Braic M *et al* 2011 *Mater. Chem. Phys.* **126** 818–25
[5] Braic M *et al* 2011 *Surf. Coat. Technol.* **206** 604–9
[6] Chen C S and Liu C P 2005 *J. Non-Cryst. Solids* **351** 3725–9
[7] Balaceanu M *et al* 2010 *Surf. Coat. Technol.* **204** 2046–50
[8] Silva E *et al* 2010 *Surf. Coat. Technol.* **205** 2134–41
[9] Balaceanu M, Braic M, Braic V and Pavelescu G 2005 *Surf. Coat. Technol.* **200** 1084–7

[10] Yao S H, Su Y L, Kao W H and Cheng K W 2005 *Mater. Lett.* **59** 3230–3
[11] Kudapa S, Narasimhan K, Boppana P and Russell W 1999 *Surf. Coat. Technol.* **120** 259–64
[12] Khan I *et al* 2010 *Nucl. Instrum. Methods Phys. Res.* B **268** 2228–34
[13] Hollstein F, Kitta D, Louda P, Pacal F and Meinhardt J 2001 *Surf. Coat. Technol.* **142** 1063–8
[14] Lai C H, Chang Y Y, Huang H L and Kao H Y 2011 *Thin Solid Films* **520** 1525–31
[15] Vasilev K *et al* 2009 *Nano Lett.* **10** 202–7
[16] Hsieh J, Tseng C, Chang Y, Chang S and Wu W 2008 *Surf. Coat. Technol.* **202** 5586–9
[17] Zhao J, Cai X, Tang H, Liu T, Gu H and Cui R 2009 *J. Mater. Sci.: Mater. Med.* **20** 101–5
[18] Akhavan O and Ghaderi E 2009 *Surf. Coat. Technol.* **203** 3123–8.
[19] Bechert T, Böswald M, Lugauer S, Regenfus A, Greil J and Guggenbichler J P 1999 *Infection* **27** 24–9
[20] Necula B S, Fratila-Apachitei L E, Zaat S A J, Apachitei I and Duszczyk J 2009 *Acta Biomater.* **5** 3573
[21] Mo A, Liao J, Xu W, Xian S, Li Y and Bai S 2008 *Appl. Surf. Sci.* **255** 435–8
[22] Jamuna-Thevi K, Bakar S, Ibrahim S, Shahab N and Toff M 2011 *Vacuum* **86** 235–41
[23] Sant S, Gill K and Burrell R 2007 *Acta Biomater.* **3** 341–50
[24] Manninen N *et al* 2011 *J. Phys. D: Appl. Phys.* **44** 375501
[25] Kótai E 1994 *Nucl. Instrum. Methods Phys. Res.* B **85** 588–96
[26] Lide D R 2004 *CRC Handbook of Chemistry and Physics* (a ready-reference book of chemical and physical data) (Boca Raton, FL: CRC Press)
[27] Grigore E, Ruset C, Li X and Dong H 2010 *Surf. Coat. Technol.* **204** 1889–92
[28] Binder S, Lengauer W, Ettmayer P, Bauer J, Debuigne J and Bohn M 1995 *J. Alloys Compounds* **217** 128–36
[29] Cunha L *et al* 2006 *Surf. Coat. Technol.* **200** 2917–22
[30] Petrov I, Barna P, Hultman L and Greene J 2003 *J. Vac. Sci. Technol.* A **21** S117
[31] Adamik M, Barna P B and Tomov I 1998 *Thin Solid Films* **317** 64–8
[32] Mulligan C and Gall D 2005 *Surf. Coat. Technol.* **200** 1495–500
[33] Kurt R, Sanjines R, Karimi A and Lévy F 2000 *Diamond Relat. Mater.* **9** 566–72
[34] Zheng W T, Cao P J, Li J J, Wang X and Jin Z S 2003 *Surf. Coat. Technol.* **173** 213–8
[35] Palacio C, Gomez-Aleixandre C, Diaz D and Garcia M 1997 *Vacuum* **48** 709–13
[36] Arias D, Arango Y and Devia A 2006 *Appl. Surf. Sci.* **253** 1683–90
[37] Graedel T 1992 *J. Electrochem. Soc.* **139** 1963
[38] Stebounova L V, Guio E and Grassian V H 2011 *J. Nanopart. Res.* **13** 233–44